Supplementary Information

Interfacial Charge Phonon Coupling in Bi_2Se_3/WSe_2 Nanohybrids for Bifunctional Near-Infrared Devices

Alka Rani[ab], Priyanka Chaudhary[a], Wei-Cheng Jhao[a], Bal Chandra Yadav*[b], Meng-Fang Lin*[a c]

[a]Department of Materials Engineering, Ming Chi University of Technology, New Taipei City, Taiwan

[b]Nanomaterials and Sensors Research Laboratory, Department of Physics, Babasaheb Bhimrao Ambedkar University, Lucknow, U.P., India

[c]Center for Plasma and Thin Film Technologies, Ming Chi University of Technology, New Taipei City, Taiwan

Corresponding Author: balchandra_yadav@rediffmail.com, mflin@mail.mcut.edu.tw

S1. Experimental details

S1.1. Materials and Methods

Selenium dioxide (SeO_2, 99.8%), bismuth nitrate pentahydrate ($Bi(NO_3)_3·5H_2O$, 98%, Thermo Scientific), sodium hydroxide (NaOH), gallic acid monohydrate (99.8%, Thermo Scientific), Triton X-100 (Sigma Aldrich), bulk WSe_2 (99.8%, Thermo Scientific), isopropanol (IPA), ethanol, acetone, deionized (DI) water, polycarbonate filter membrane (0.4 µm pore size, 47 mm diameter, Merck Isopore), Kapton tape (polyimide), and Aluminum tape were used in this study.

S1.2. Synthesis method

As shown in **Figure S1(a)**, Bi_2Se_3 was synthesized via a hydrothermal method. First, sodium hydroxide (NaOH,1.28 g) was dissolved in 50 mL of deionized (DI) water under magnetic stirring at 70ºC for 10 minutes. Subsequently, selenium dioxide (SeO_2, 0.47g) and bismuth nitrate pentahydrate ($Bi(NO_3)_3·5H_2O$, 1.38 g) were added sequentially, followed by continuous stirring for 20 minutes. Then, gallic acid (1.34 g) was added to the solution, along with 50 µL of Triton X-100. The pH of the final mixture was adjusted to

~12, and the reaction was maintained under stirring for 4 hours. The resulting solution was transferred into a Teflon-lined stainless-steel autoclave and heated at 200 °C for 24 hours. After naturally cooling to room temperature, the obtained precipitate was collected by centrifugation, washed 5 times with DI water and ethanol, and dried at 60ºC. Finally, the powder was annealed at 400 °C for 2 hours under vacuum conditions to enhance the crystallinity. As shown in **Figure S1(b)**, few-layer WSe_2 nanosheets were prepared via a mechanical exfoliation process. Specifically, 1 g of bulk WSe_2 powder was dispersed in 30 ml of isopropanol and subjected to ultrasonication for 9 hours to exfoliate the layered structure, as shown in Figure S1b. The dispersion was then centrifuged to remove unexfoliated particles, and the supernatant, containing exfoliated WSe_2 nanosheets, was collected and dried at 80°C for 8 hours. As presented in **Figure S1(c)**, the Bi_2Se_3/WSe_2 nanohybrids were synthesized by thoroughly grinding the exfoliated WSe_2 nanosheets with as-prepared Bi_2Se_3 powder using a mortar and pestle to form a homogeneous mixture. The blended material was subsequently annealed at 400ºC for 2 hours under vacuum, yielding the final Bi_2Se_3/WSe_2 nanohybrid.

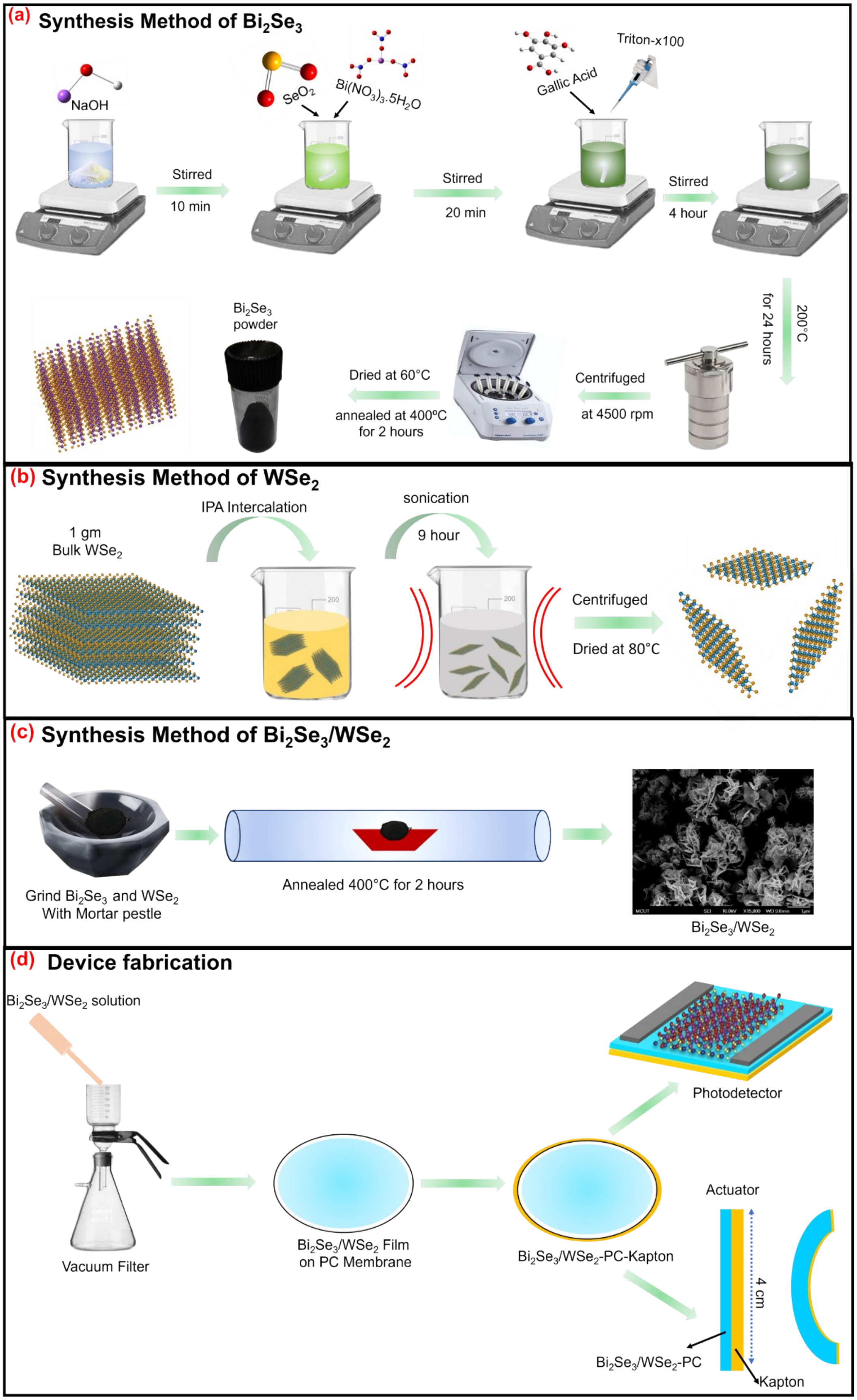
(a) Synthesis Method of Bi_2Se_3
NaOH
SeO_2
$Bi(NO_3)_3.5H_2O$
Gallic Acid
Triton-x100
Stirred
10 min
Stirred
20 min
Stirred
4 hour
200°C
for 24 hours
Centrifuged
at 4500 rpm
Dried at 60°C
annealed at 400°C
for 2 hours
Bi_2Se_3
powder
(b) Synthesis Method of WSe_2
1 gm
Bulk WSe_2
IPA Intercalation
sonication
9 hour
200
Centrifuged
Dried at 80°C
(c) Synthesis Method of Bi_2Se_3/WSe_2
Grind Bi_2Se_3 and WSe_2
With Mortar pestle
Annealed 400°C for 2 hours
Bi_2Se_3/WSe_2
(d) Device fabrication
Bi_2Se_3/WSe_2 solution
Vacuum Filter
Bi_2Se_3/WSe_2 Film
on PC Membrane
Bi_2Se_3/WSe_2-PC-Kapton
Photodetector
Actuator
4 cm
Bi_2Se_3/WSe_2-PC
Kapton

Figure S1. Synthesis Procedure of (a) Bi_2Se_3, (b) Exfoliated WSe_2, (c) Bi_2Se_3/WSe_2 nanohybrid. (d) Device fabrication of the actuator and photodetector.

S1.3. Device Fabrication The device fabrication procedure is shown in **Figure S1(d).** Rapid near-infrared (NIR) responsive actuators were developed by leveraging the mismatch in thermal expansion. First, a polycarbonate Bi_2Se_3/WSe_2-PC composite was prepared as the upper layer of the actuator. Due to the high coefficient of thermal expansion of the PC membrane (~98 ppm/K), the photothermal conversion properties of modified WSe_2 nanosheets were utilized to generate effective thermal actuation. The resulting PC-Bi_2Se_3/WSe_2 composite exhibited rapid photothermal conversion and efficient heat transfer pathways. The interconnected nanosheet network of Bi_2Se_3/WSe_2 facilitated rapid heat transfer to cooler surrounding regions upon NIR irradiation. Kapton, characterized by a low coefficient of thermal expansion of nearly 20 ppm/k[1], was employed as the bottom layer. By combining the Bi_2Se_3/WSe_2-PC composite with Kapton, a flexible actuator was constructed. Upon NIR light irradiation, the actuator bent away from the light source due to differential expansion and reverted to its original shape when the light was turned off, demonstrating excellent, fast, and reversible actuation performance. This responsive behavior is largely attributed to the strong NIR absorption and photothermal conversion capability of the Bi_2Se_3/WSe_2 nanohybrids. Following the compressive chemical and physical processes, a bifunctional device was further fabricated to serve as both a photodetector and actuator, capable of detecting varying NIR power levels. Nanohybrid powders of Bi_2Se_3/WSe_2 at various mass ratios were prepared (1:1, 1:2, 1:3, 2:1, 3:1). The various compositions were achieved by fixing the mass of one component (Bi_2Se_3 or WSe_2) at 0.25 g and adjusting the mass of the other components to obtain the target ratio. Each mixture was dissolved in 30 mL of DI water. To form a stable suspension, it was first subjected to ultrasonication for 2 hours, followed by continuous magnetic stirring overnight. For the fabrication of each composite membrane, a uniform volume of 15 mL of the final nanohybrid solution was isolated and vacuum-filtered using a PC filter membrane with a pore size of 0.22 μm and a thickness of 150 μm for 3 hours. The resulting film was dried at 80ºC for 4 hours. To complete the actuator structure, commercial Kapton tape was firmly laminated onto the Bi_2Se_3/WSe_2-

PC film, creating a flexible actuator. The dried composite film was then cut into actuator strips (length: 4 cm; varying widths) for actuation testing. For performance evaluation, each actuator strip was fixed at one end and vertically positioned in front of the NIR light source. Aluminum Tape was applied on the surface of the Bi_2Se_3/WSe_2 layer to serve as electrodes for photodetection measurements. Bending angle of this soft actuator was quantified by measuring the angular change from the initial position to the deformed state using a protractor, with motion captured via a video camera.

S2. Characterization Techniques

Surface morphology was examined using a scanning electron microscope (SEM; Hitachi, Model S-3400N) operated at an accelerating voltage of 15 kV. Raman spectroscopy (Horiba, Model IHR 550) with a 532 nm excitation wavelength was employed to examine the vibrational modes of the materials. Fourier-transform infrared spectroscopy (FT-IR; PerkinElmer, Model Spectrum) was used to identify the functional groups present on the surface of the Bi_2Se_3/WSe_2 nanohybrids. For external stimulation, an NIR light source (Philips, Model PH070004) and a DC power supply (Hila Model DP-30052) were used. The power density of the NIR light was measured using a Linsang NIR power meter (Model LS122 IR). Actuator motion was recorded using a video camera, with angle tracked by a protractor and a laser displacement sensor (Keyence Model LK-H080). Temperature variations during actuation were monitored using a thermal imaging camera (Perfect Prime, Model IR0019). Photodetection performance was measured from the Keithley electrometer (Model 6517B).

S3 Results and Discussion

Figure S2(a) displays a SEM micrograph of the WSe_2 nanostructure, revealing its characteristic 2D, sheet-like morphology. The nanosheets exhibit a flat, thin, and few-layered structure with smoothly folded edges. Numerous overlapping sheets are evident on the surface, contributing to a high specific surface area that enhances the transport of electrons. As shown in **Figure S2(b)**, the SEM image of Bi_2Se_3 exhibits a flower-like aggregation of ultrathin nanoflakes arranged in a petal-like configuration. These hierarchical structures form well-defined nanoflowers, indicating successful morphological control during the synthesis process. As depicted in **Figure S2(c)**, the

Bi_2Se_3/WSe_2 nanohybrid successfully retains its original flower-like morphology of Bi_2Se_3 while integrating WSe_2 nanosheets. The attachment of Bi_2Se_3 nanoflowers to the surface of WSe_2 forms a cauliflower-like hybrid nanostructure, suggesting strong interfacial interaction between the two components. **Figure S2(d)-(f)** presents TEM images of WSe_2, Bi_2Se_3, and the Bi_2Se_3/WSe_2 nanohybrid, respectively, all at a scale of 100 nm. The TEM image of WSe_2 in **Figure S2(d)** and **(e)** confirms a thin, planar hexagonal sheet-like morphology, highlighted by the yellow dotted line. The measured lattice fringe spacing of 0.287 nm corresponds to the (002) planes of WSe_2, consistent with the XRD results. The SAED pattern shown in **Figure S2(g)** exhibits well-defined diffraction spots, confirming the single-crystalline nature of WSe_2. The measured interplanar spacing of 0.306 nm matches the (101) plane of rhombohedral Bi_2Se_3. The corresponding SAED pattern (Figure S2h) displays multiple concentric rings, indicating the polycrystalline nature of the sample. These rings can be indexed to the (015), $(01\underline{11})$, (202), $(02\underline{10})$, and $(21\underline{10})$ planes of the Bi_2Se_3. **Figure S2(f)** shows the TEM image of the Bi_2Se_3/WSe_2 nanohybrid. The observed lattice fringes reveal interplanar spacing of 0.498 nm and 0.311 nm, corresponding to WSe_2 and Bi_2Se_3, respectively. These results further confirm the successful formation of the nanohybrid and the preservation of the crystallinity of both constituents.

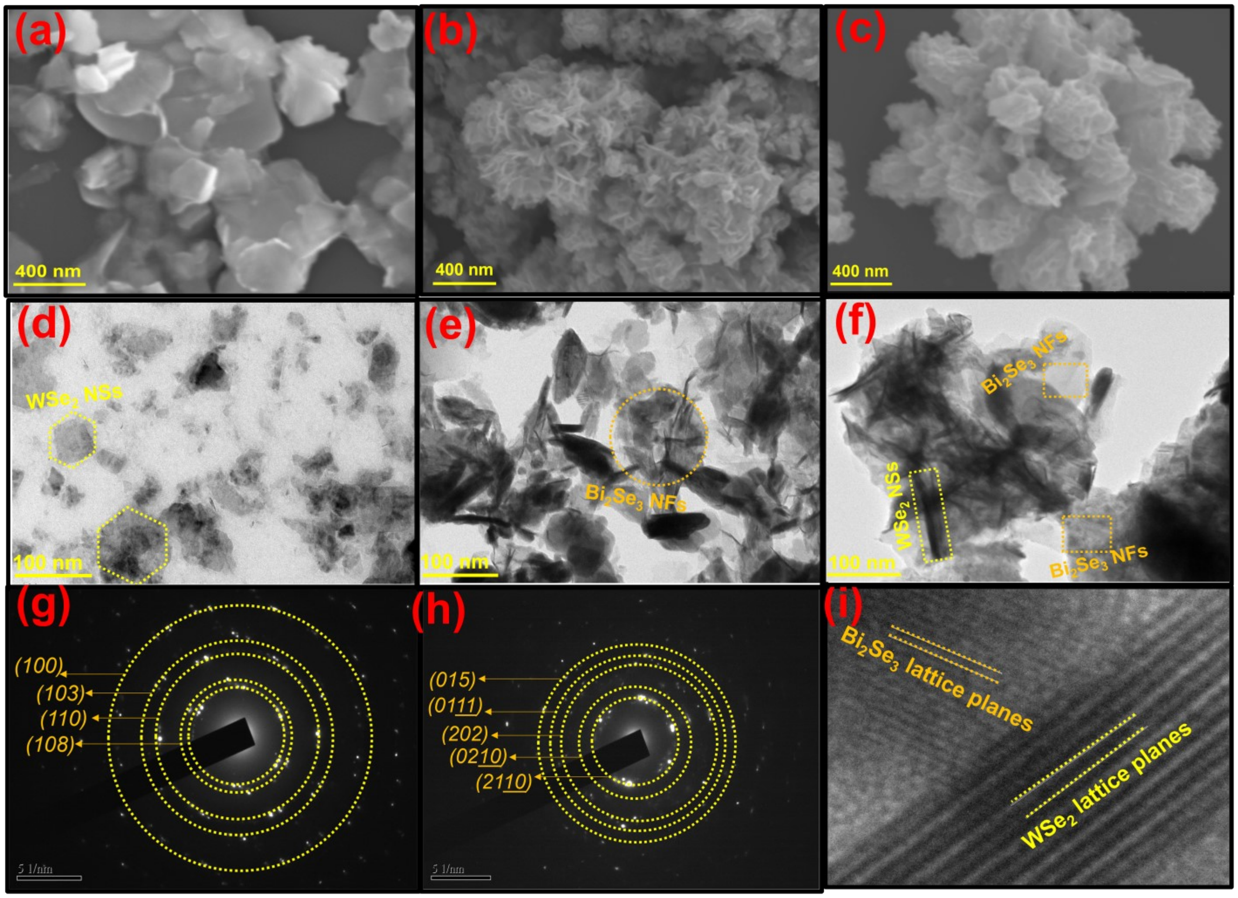

Figure S2. SEM images at a 400 nm scale of materials, (a) $WSe_{2,}$ (b) $Bi_2Se_{3,}$ (c) Bi_2Se_3/WSe_2. TEM images at a 100 nm scale of materials, (d) $WSe_{2,}$ (e) $Bi_2Se_{3,}$ (f) Bi_2Se_3/WSe_2. SAED pattern of (g) $WSe_{2,}$ (h) Bi_2Se_3. (i) Representation of Bi_2Se_3 and WSe_2 lattice planes in Bi_2Se_3/WSe_2 nanohybrid.

To further elucidate the chemical composition within the domains of WSe_2, and Bi_2Se_3, EDS elemental mapping was performed on the Bi_2Se_3/WSe_2 shown in **Figure S3a**. The mapping results reveal a nearly uniform distribution of W, Se, and Bi across the domains. Selenium distribution is red in color which is uniform and intense across the entire region. This indicates Se rich composition. The EDS spectrum obtained from the mapped region shows characteristic peaks of Bi, W, and Se. This confirms the presence of WSe_2 and Bi_2Se_3 within the mapped domains, which approves the formation of Bi_2Se_3/WSe_2 nanohybrid. Furthermore, the EDS elemental spectra obtained by TEM presented in the supplementary **Figure S3b**, show good compatibility with the composition of Bi_2Se_3/WSe_2

nanohybrid. **Figure S3b(i)** shows the EDS spectrum of Bi_2Se_3 while **Figure S3b(ii)** represents the EDS spectrum of WSe_2 present in Bi_2Se_3/WSe_2 nanohybrid. These regions are identified in **Figure S3b(iii)** where the marked areas correspond to the locations from which the spectra were collected. The region marked 8-1-1 corresponds to the Bi_2Se_3 flakes, while the region indicated as 8-1-2 represents the WSe_2 nanostructures, confirming the presence of both in the Bi_2Se_3/WSe_2 nanohybrid.

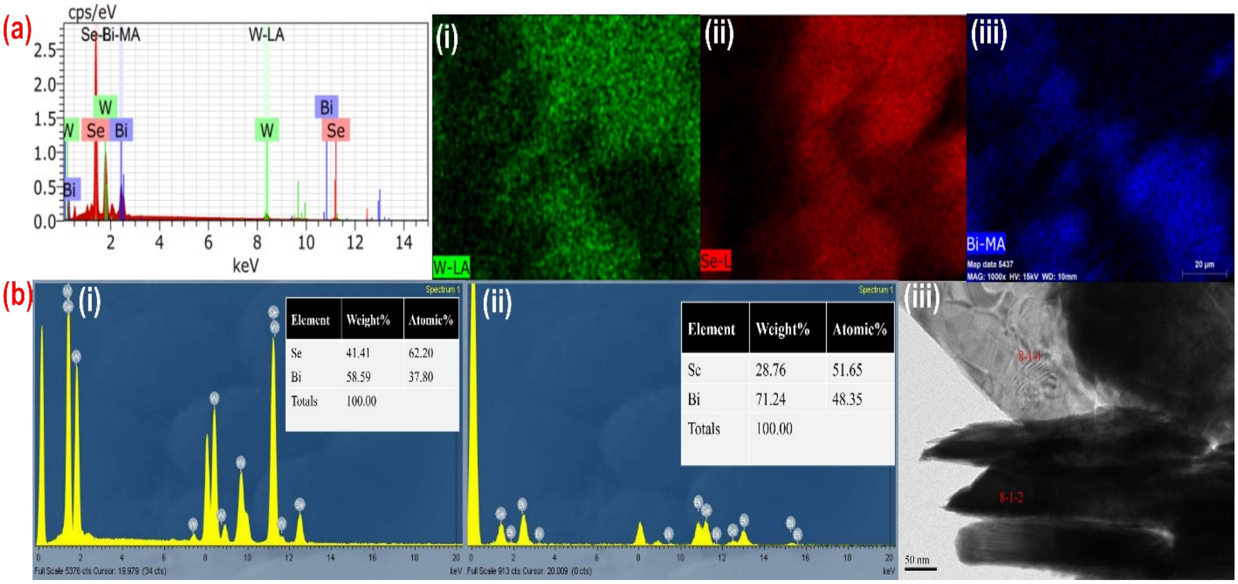

Element	Weight%	Atomic%
Se	41.41	62.20
Bi	58.59	37.80
Totals	100.00	

Element	Weight%	Atomic%
Se	28.76	51.65
Bi	71.24	48.35
Totals	100.00	

Figure: S3 (a) Elemental mapping showing homogeneous distribution of Bi, W and Se located on as prepared Bi_2Se_3/WSe_2 nanohybrid. (b) EDS Spectra of Bi_2Se_3/WSe_2 nanohybrid.

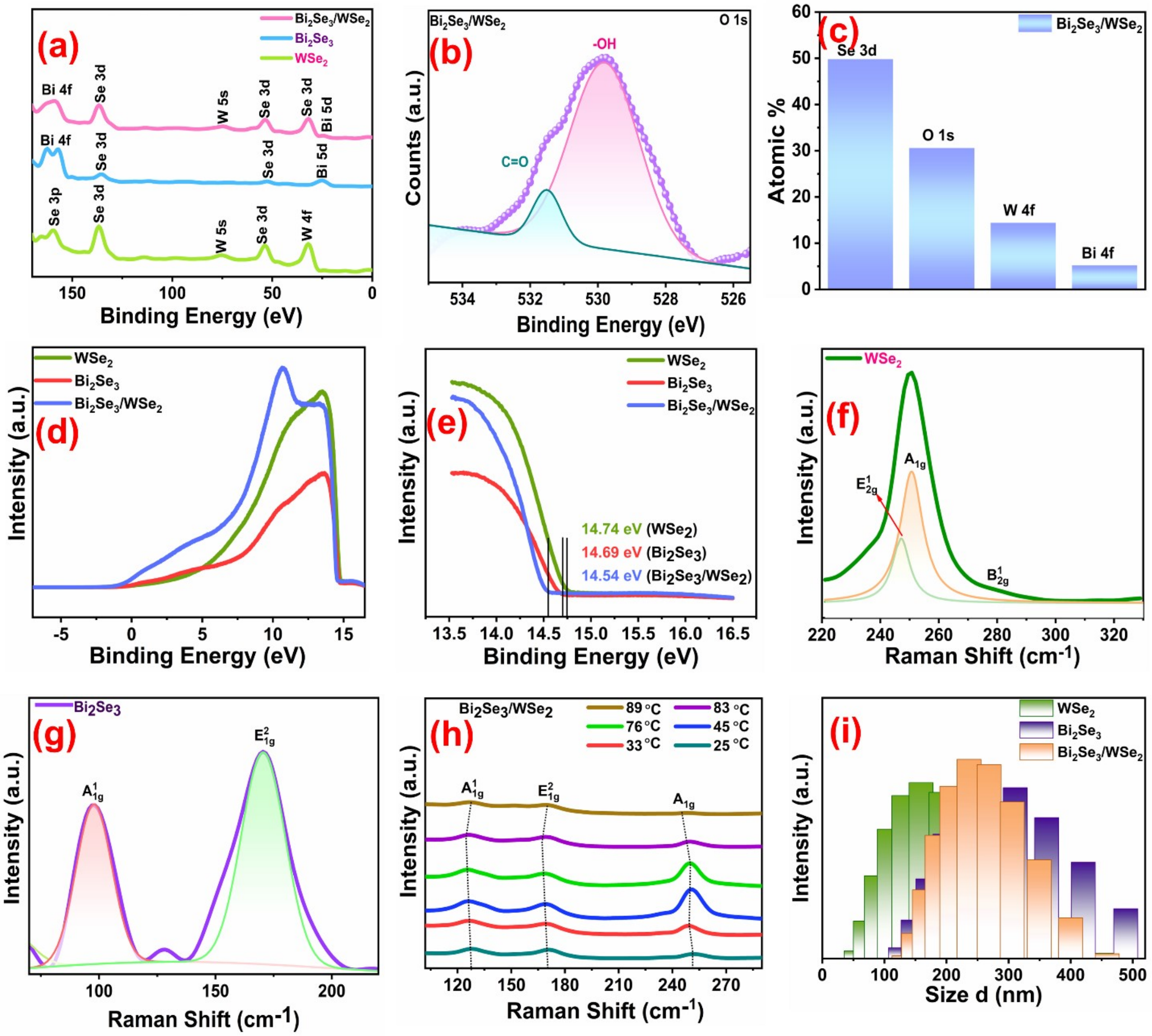

Figure S4. (a) XPS survey spectrum of WSe$_2$, Bi$_2$Se, and Bi$_2$Se$_3$/WSe$_{2,}$ confirming the presence of W, B, and Se. (c) Surface elemental percentage of Bi, W, Se, and O calculated by XPS. (d) Full range UPS spectrum of all samples WSe$_2$, Bi$_2$Se$_3$, and Bi$_2$Se$_3$/WSe$_2$. (e) UPS binding energy profiles showing the secondary electron cut off energy. Raman spectrum of (f) WSe$_{2,}$ (g) Bi$_2$Se$_3$. (h) Raman spectra of Bi$_2$Se$_3$/WSe$_2$ nanohybrid at different temperatures. (i) DLS histogram of WSe$_2$, WSe$_2$ and Bi$_2$Se$_3$/WSe$_2$ nanohybrid.

In pristine WSe$_2$, the W 4f spectrum shows two peaks at 30.75 eV (W4f$_{7/2}$) and 32.91 eV (W 4f$_{5/2}$), confirming the W^{4+} oxidation state associated with W-Se bonding. A small peak at 36.48 eV suggests minor surface oxidation (WO_x species). The Se 3d spectrum shows two prominent peaks at 52.98 eV and 53.72 eV, corresponding to the Se $3d_{5/2}$ and Se $3d_{3/2}$ states, confirming selenium's presence in WSe_2. Further, the Se element state 3d spectrum of pristine Bi_2Se_3 reveals two distinct peaks: Se-I at 52.28 eV, attributed to Bi-Se bonds, and Se-II at 53.94 eV, corresponding to Se-Se bonds, likely present due to slight non-stoichiometry or surface states. The Bi 4f spectrum shows peaks at 156.32 eV and 161.61 eV assigned to Bi^{3+} (Bi $4f_{7/2}$ and Bi $4f_{5/2}$). Additional peaks observed at 157.54 eV and 162.78 eV are indicative of surface oxidation of Bi_2Se_3. The spin-orbit splitting of 5.29 eV between Bi $4f_{7/2}$ and Bi $4f_{5/2}$ aligns well with reported values for Bi_2Se_3, confirming its oxidation state and purity. The complete survey, shown in **Figure S4(a)**, displays the pure formation of synthesized materials, with the presence of atoms and their corresponding binding energies. As shown in **Figure S4(b),** the O 1s spectra of Bi_2Se_3/WSe_2 exhibit peaks at 532.30 eV, 532.29 eV, and 531.50 eV, respectively, which are typically attributed to adsorbed oxygen or water molecules-a common observation in samples exposed to ambient air. The atomic weight percentage of surface elements present in the Bi_2Se_3/WSe_2 nanohybrid is presented in **Figure S4(c)** with the highest atomic % Se in the 3d state.

In UPS (**Figure S4d and e**), the measurement of work function using the width of the photoemission spectrum, that is, from the secondary electron cut off to the Fermi edge, as presented in the Equations S(**1)** and **(2**).[2]

$$\phi = h\nu - K.E_{max} \qquad (S1)$$

$$\phi = h\nu - (E_{SEC} - E_F) \qquad (S2)$$

Where ϕ, h, $\boldsymbol{v}$, E_{SEC}, and E_F are the work function, Planck's constant, frequency of Ultraviolet light, onset energy or cut-off energy of secondary electrons, and Fermi level, respectively.

By the UV-visible spectroscopy, the absorption coefficient can be determined by Equations S **(3)** and **(4**)

$$\alpha = 2.303\frac{A}{t} \qquad (S3)$$

Where t is the thickness. The theory of optical absorption defines the relationship between the absorption coefficient and the photon energy for direct allowed transitions, as in Equation S**4**

$$\alpha hv = A(hv - E_g)^{\frac{1}{2}} \quad \text{(S4)}$$

Where A is the constant, E_g shows the band gap, and h$\boldsymbol{v}$ represents the photon energy. The band gap E_g can be determined by extrapolating the linear region of the $(\alpha h\boldsymbol{v})^2$ versus h$\boldsymbol{v}$ plot is extrapolated at α=0. **Figure S4f and g**, represent the Raman spectrum of pure WSe_2 and pure Bi_2Se_3. Raman spectra of Bi_2Se_3/WSe_2 nanohybrid at different temperatures is presented in **Figure 4h**. **Figure S4i**, shows the particle size obtained using the DLS technique, all the values ranging between for WSe_2, Bi_2Se_3, and Bi_2Se_3/WSe_2 nanohybrid is 92-488 nm, 125-568 nm, and 92-420 nm respectively.

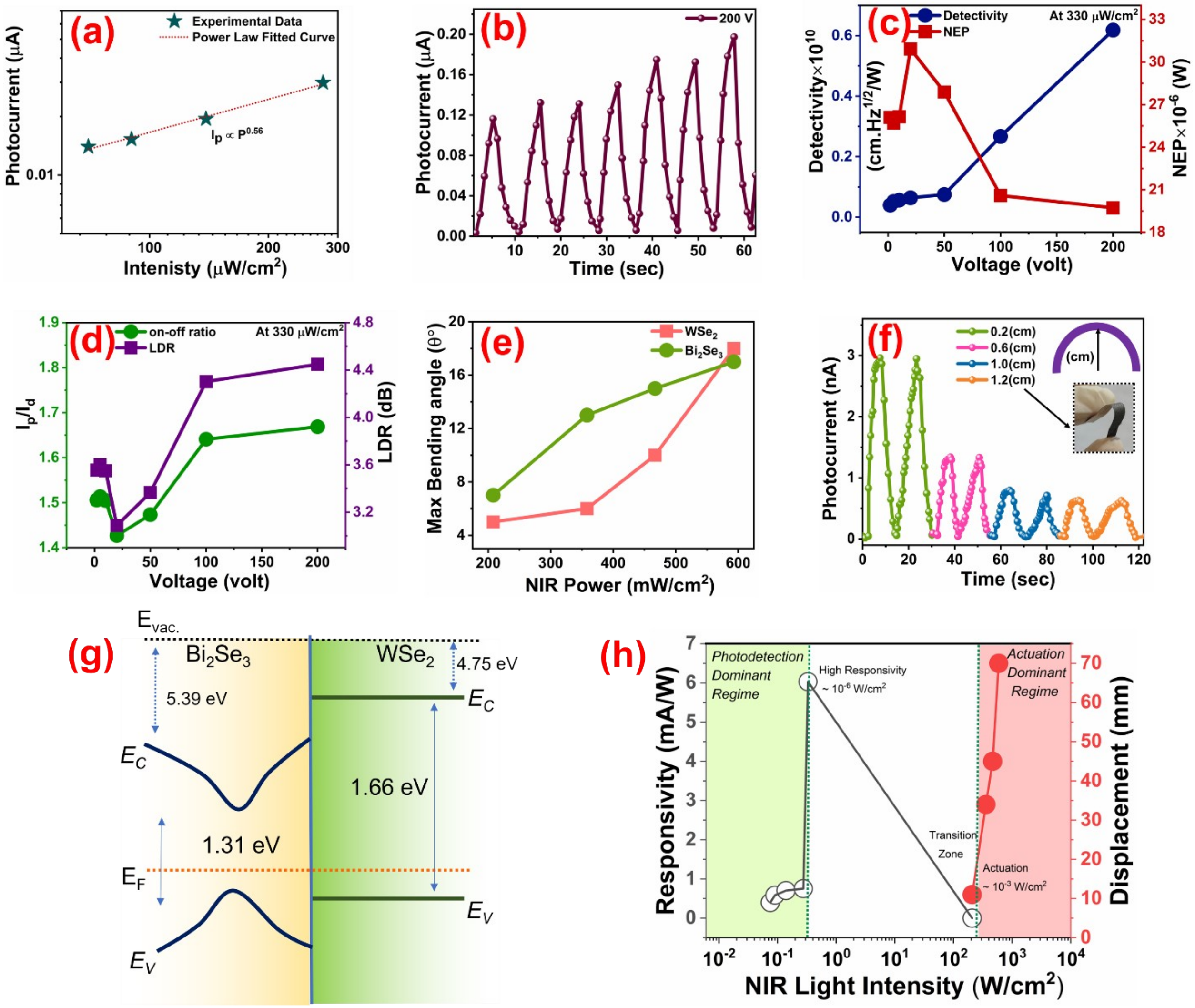

Figure S5. (a) Power-dependent photocurrent of the device at 200 V bias under NIR illumination. (b) Transient photo response of PD at 200V under 330 μW/cm^2. (c,d) Detectivity, NEP, on/off ratio, and LDR under 330 μW/cm^2 at different bias potentials for Bi_2Se_3/WSe_2 nanohybrid. (e) Flexibility test of PD under 330 μW/cm^2. (f) Actuation performance of Bi_2Se_3 and WSe_2 actuators of 3 mm width in response to different light stimulation intensities. (g) Energy band diagram of Bi_2Se_3/WSe_2 nano-heterojunctions showing the VB and CB. (h) An intensity-dependent phase diagram clearly indicates the threshold between sensing-dominant and actuation-dominant regimes.

The relationship between the photocurrent and light intensity, as in a power law function, is shown in **Figure S5(a)**. **Figure S5(b)** depicts the transient photo response of PD at

200V under 330 μW/cm[2]. Responsivity, defined as the photocurrent generated per unit incident optical power on the active device area, is expressed as equation **S5**:[3]

$$R = \frac{I_{light} - I_{dark}}{P \cdot A} \tag{S5}$$

Where I_{light} and I_{dark} denote the current under illumination and in the dark, respectively. P is the incident light intensity, and A is the photo-absorbing active area of the device.

The specific detectivity (D), a critical parameter reflecting the ability to detect weak signals, was extracted using equation **S6**:[4]

$$D = \frac{R \cdot A^{\frac{1}{2}}}{(2qI_d)^{1/2}} \tag{S6}$$

where q is the elementary charge and I_d is the dark current. This power-dependent trend is also evident in responsivity, detectivity, and linear dynamic range (LDR). The LDR, a critical figure of merit for image sensors, is expressed as equation **S7**:[5]

$$LDR = 20\log\left(\frac{J_{upper}}{J_{lower}}\right) \tag{S7}$$

where J represents the current density. The upper limit corresponds to the deviation from linear photocurrent response, typically governed by slower carrier transit times.[6] **Figure S5c** and **d** represent the detectivity, NEP, on-off ratio, and LDR of the PD device at different bias potentials under NIR illumination of intensity 330 μW/cm[2] Bi_2Se_3/WSe_2 nanohybrid. As represented in **Figure S5e**, The I-t curves were recorded under different bending conditions at an applied bias of 200 V and an illumination intensity of 330 μW/cm[2] to evaluate the flexibility of the device. **Figure S5e** demonstrates the time-dependent response of the flexible device's photocurrent under periodic illumination at various bending radii. The flexible device shows distinct ON/OFF switching characteristics under various bending states. It is also interesting to see that the photocurrent increases when the bending radius decreases. The highest response is observed when the radius is 0.2 cm. It is possible that the strain effect enhances the charge of transport and separation at the interface. A band diagram of the Bi_2Se_3 and WSe_2 nano-heterojunctions formed within the Bi_2Se_3/WSe_2 nanohybrid is shown in **Figure S5(g).** As shown in **Figure S5h,** we have plotted a phase diagram featuring three distinct regions: the photodetection-dominant regime, the transition zone, and the actuation-dominant regime. In the first region, the photodetection dominant regime, the responsivity increases as the light intensity level rises from 75 µW/cm² to 330 µW/cm² at low intensity (µW order). As the intensity increases into the high-intensity region (mW order), at 208 mW/cm², the photoresponsivity begins to decrease. At such high intensities, thermally generated electron-hole pairs become highly active, which increases the dark current and concurrently increases the device's temperature. This temperature rise is utilized for photothermal actuation, effectively transforming the device into an actuator. Consequently, in the actuation dominant regime, spanning 208 mW/cm^2 to 593 mW/cm^2. We analyzed the performance as an actuator, achieving a maximum bending angle of 70°. Above this intensity, the device suffers from material defects and ultimately burns out.

Table S1: Photodetection performance of parameter of Bi_2Se_3/WSe_2

Ip (A)	**Id (A)**	**On-off ratio**	**Responsivity (A/W)**	**Detectivity (cm·Hz$^{1/2}$/W)**	**NEP (W)**	**LDR (dB)**	**Voltage (Volt)**
1.99×10^{-7}	1.19×10^{-7}	1.67	**6.03**$\times10^{-3}$	6.18×10^{9}	1.97×10^{-5}	4.45	200
3.97×10^{-8}	2.42×10^{-8}	1.64	1.17×10^{-3}	2.67×10^{9}	2.06×10^{-5}	4.30	100
5.14×10^{-9}	3.49×10^{-9}	1.47	1.25×10^{-4}	7.49×10^{8}	2.79×10^{-5}	3.3	50
4.49×10^{-9}	3.15×10^{-9}	1.43	1.02×10^{-4}	6.41×10^{8}	3.09×10^{-5}	3.09	20
2.63×10^{-9}	1.75×10^{-9}	1.50	6.68×10^{-5}	5.65×10^{8}	2.61×10^{-5}	3.55	10
2.17×10^{-9}	1.43×10^{-9}	1.51	5.58×10^{-5}	5.21×10^{8}	2.57×10^{-5}	3.60	5
1.30×10^{-9}	8.60×10^{-10}	1.51	3.30×10^{-5}	3.97×10^{8}	$2.61\times10^{-}$	3.56	2

S4. Photothermal performance

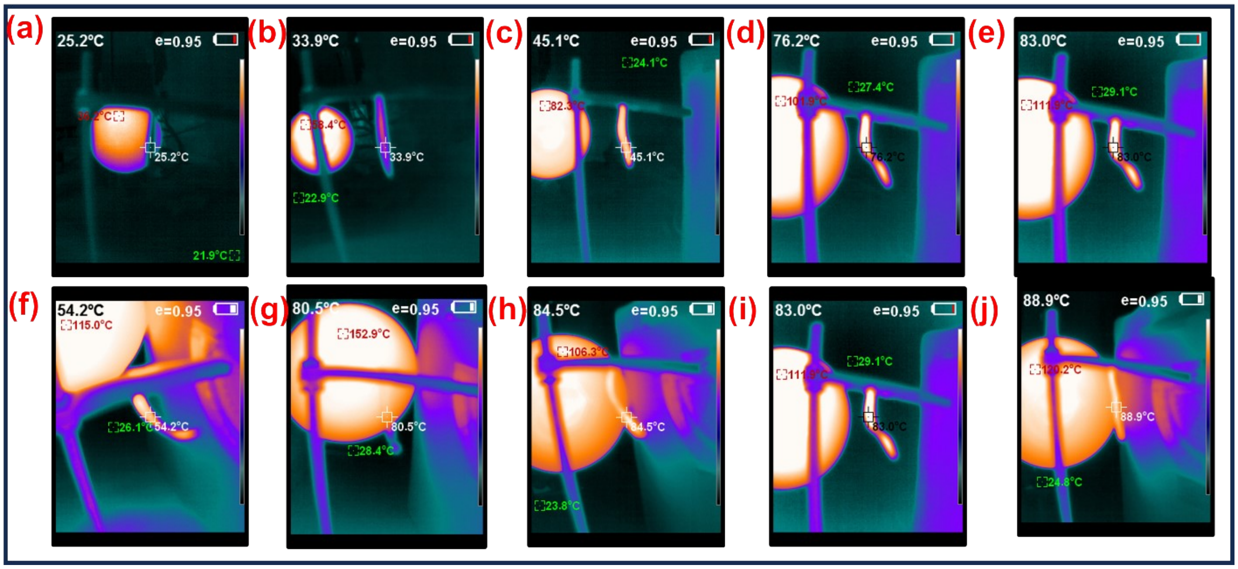

Figure S6. Temperature infrared images of the actuator (1:3) of 3 mm when exposed to different intensities of infrared light. (a) Dark, (b) 208, (c) 358, (d) 467, and (e) 593 mW/cm².Temperature infrared images of Bi_2Se_3/WSe_2 actuator (3 mm) when exposed to 593 mWcm^{-2} intensity near infrared light. (f) 1:1, (g) 1:2, (h) 1:3, (i) 2:1, and (j) 3:1.

The photothermal conversion efficiencies of the Bi_2Se_3, WSe_2, and the Bi_2Se_3/WSe_2 films were calculated using the following photothermal conversion efficiency equation S8

$$\eta = \frac{Cm\Delta T}{Pst} \times 100\ \% \qquad \text{(S8)}$$

where ŋ represents the photothermal conversion efficiency. C is the specific heat capacity. It quantifies how much heat must be delivered to a substance to heat it over a temperature range [10]. we have incorporated literature values of C for the individual components; 147.3 J/mol K[11] for WSe_2, 160 J/mol K[12] for Bi_2Se_3, 153 J/mol K (Bi_2Se_3/WSe_2), for Bi_2Se_3/WSe_2 we estimate an average value. m is the mass of the film, and is the change in the film temperature during irradiation, P corresponds to the power density of the incident NIR light, S is the effective illuminated area of the film surface, and t is the exposure time under illumination. calculated photothermal conversion efficiencies for Bi_2Se_3, WSe_2, and the Bi_2Se_3/WSe_2 are 12 %, ~ 15%, 29.6% respectively. The incident power density was maintained at 593 mW/cm^2 during irradiation. Under these conditions the temperature of the WSe_2, Bi_2Se_3, and Bi_2Se_3/WSe_2 nanohybrid films increased within 7 sec, 8 sec and within 7 sec. The maximum temperature for WSe_2 and Bi_2Se_3 was 60ºC and 64º C.

Table S2: Performance parameters of TMDCs and Bi_2Se_3 as a photodetector and light-driven actuator

Material	Photocurrent (nA)	Detectivity (cm·Hz$^{1/2}$/W)	Max Displacement/ angle	Max Temperature (°C)	Intensity (mW/cm²)	References
WS_2-PNiPAM	-	-	7 mm	70	8000 (NIR)	7
Bi_2Se_3	~110	3.3×10^{10}	-	-	142.93 (NIR)	8
WSe_2 single crystal	~938×10^3	10^7	-	-	3 (Visible)	9
GO	-	-	1.6 cm^{-1}	102	600 (NIR)	10
MoS_2-PI	-	-	~70°	148	148 (Sunlight)	11
PDMS/WS_2	-	-	23.99°		300 (NIR)	12
WSe_2-graphene/PDMS	-	-	~82°	142	970 (NIR)	13
WSe_2	~ 160	3.03×10^{11}	-	-	105 (Visible)	14
WSe_2, Au contact	~80	2.26×10^{11}	-	-	8 (Visible)	15
$Bi_2Se_3/ReSe_2$	265×10^{-6}	1.1×10^{11}	-	-	1,600 (Visible)	16

Bi_2Se_3/WSe_2	**199**	**6.18×10^9**	**70°**	**88.9**	**0.330 (NIR)**	**Our work**

References:

1. Grein, M.; Gerstenberg, J.; von der Heide, C.; Bandorf, R.; Bräuer, G.; Dietzel, A., Niobium-containing DLC coatings on various substrates for strain gauges. *Coatings* **2019,** *9* (7), 417.
2. Chang, C.; Lee, C.-Y.; Tai, N.-H., Human exhalation CO_2 sensor based on the PEI-PEG/ZnO/NUNCD/Si heterojunction electrode. *ACS omega* **2022,** *7* (18), 15657-15665.
3. Rani, A.; Verma, A.; Yadav, B. C., Plasmon resonance enhanced Pd-decorated hybrid tungsten disulfide (WS_2) multi-wavelength ultra-responsive photodetector. *Tungsten* **2025,** *7* (2), 374-392.
4. Singh, R.; Patel, C.; Kumar, P.; Dubey, M.; Sriram, S.; Mukherjee, S., High detectivity and fast MoS_2 monolayer MSM photodetector. *ACS Applied Electronic Materials* **2022,** *4* (12), 5739-5746.
5. Lin, Q.; Armin, A.; Lyons, D. M.; Burn, P. L.; Meredith, P., Low noise, IR-blind organohalide perovskite photodiodes for visible light detection and imaging. *Adv. Mater* **2015,** *27* (12), 2060-2064.
6. Armin, A.; Juska, G.; Philippa, B. W.; Burn, P. L.; Meredith, P.; White, R. D.; Pivrikas, A., Doping-Induced Screening of the Built-in-Field in Organic Solar Cells: Effect on Charge Transport and Recombination. *Advanced Energy Materials* **2013,** *3* (3), 321-327.
7. Zong, L.; Li, X.; Han, X.; Lv, L.; Li, M.; You, J.; Wu, X.; Li, C., Activation of actuating hydrogels with WS_2 nanosheets for biomimetic cellular structures and steerable prompt deformation. *ACS Applied Materials Interfaces* **2017,** *9* (37), 32280-32289.
8. Wang, F.; Li, L.; Huang, W.; Li, L.; Jin, B.; Li, H.; Zhai, T., Submillimeter 2D Bi_2Se_3 flakes toward high-performance infrared photodetection at optical communication wavelength. *Advanced Functional Materials* **2018,** *28* (33), 1802707.
9. Dixit, V.; Nair, S.; Joy, J.; Vyas, C. U.; Patel, A. B.; Chauhan, P.; Sumesh, C. K.; Narayan, S.; Jha, P. K.; Solanki, G. K., Growth and application of WSe_2 single crystal synthesized by DVT in thin film hetero-junction photodetector. *The European Physical Journal B* **2019,** *92* (6), 118.
10. Weng, M.; Xiao, Y.; Yao, L.; Zhang, W.; Zhou, P.; Chen, L., Programmable and self-healing light-driven actuators through synergetic use of water-shaping and-welding methods. *ACS Applied Materials Interfaces* **2020,** *12* (49), 55125-55133.
11. Ji, Q.; Jing, Z.; Shen, J.; Hu, Y.; Chang, L.; Lu, L.; Liu, M.; Liu, J.; Wu, Y., Dual-Responsive Soft Actuators with Integrated Sensing Function Based on 1T-MoS_2 Composite. *Advanced Intelligent Systems* **2021,** *3* (7), 2000240.
12. Chen, J.; Zhang, K.; Shi, X.; Huang, Y.; Jiang, B., Bioinspired polysiloxane/WS_2 composites with stretchable and near-infrared light remote-controlled self-healing abilities for deployable deformation actuators. *Composites Science Technology* **2023,** *244*, 110297.

13. Su, Z.; Zhao, Y.; Huang, Y.; Xu, C.; Yang, X.; Wang, B.; Xu, B.; Xu, S.; Bai, G., Light-driven soft actuator based on graphene and WSe_2 nanosheets composite for multimodal motion and remote manipulation. *Nano Research* **2023,** *16* (1), 1313-1319.

14. Zhu, Y.; Ni, S.; Zhu, F.; Hu, Z.; Pan, C.; Fan, X.; Ma, Y.; Mi, S.; Liu, C.; Tang, W., Photocurrent Generation and Collection in a WSe_2-Based Composite Detector. *Coatings* **2025,** *15* (6), 672.

15. Ryoo, S.; Sim, J.; Jeong, S.; Jang, J.; Woo, J.; Park, J.; Ko, S.; Kim, Y.; Song, Y.; Yoo, J., Noise-Reduced WSe_2 Phototransistors for Enhanced Photodetection Performance via Suppression of Metal-Induced Gap States. *Advanced Materials Technologies* **2025,** *10* (9), 2500064.

16. Yun, W.; Peng, W.; Li, L.; He, T.; Wanyu, M.; Xu, T.; Bingwang, Y.; Shulin, S.; Caixia, K.; Mingming, J. In *High-Performance Self-Powered Broadband Photodetectors Based on a Bi_2Se_3 Topological Insulator/$ReSe_2$ Heterojunction for Signal Transmission*, Photonics, MDPI AG: 2025; p 709.